Atmos. Meas. Tech. Discuss., 5, 4599–4633, 2012
www.atmos-meas-tech-discuss.net/5/4599/2012/
doi:10.5194/amtd-5-4599-2012

Atmospheric Measurement Techniques Discussions

Volcanic SO_2 and SiF_4 visualization using 2-D thermal emission spectroscopy – Part 2: Wind propagation and emission fluxes

A. Krueger[1,2], W. Stremme[1], R. Harig[2], and M. Grutter[1]

[1]Centro de Ciencias de la Atmósfera, Universidad Nacional Autónoma de México, Mexico City, Mexico
[2]Technische Universität Hamburg-Harburg, Hamburg, Germany

Received: 24 April 2012 – Accepted: 14 June 2012 – Published: 3 July 2012

Correspondence to: M. Grutter (grutter@unam.mx)

Published by Copernicus Publications on behalf of the European Geosciences Union.

Abstract

The technique for measuring two-dimensional (2-D) plumes of volcanic gases with thermal emission spectroscopy was described in Part 1 by Stremme et al. (2012). In that paper the instrumental aspects as well as retrieval strategies for obtaining the slant column images of SO_2 and SiF_4, as well as animations of particular events observed at the Popocatépetl volcano, were presented. This work focuses on the procedures for determining the propagation speed of the gases and estimating an emission flux from the given image sequences. A 2-D column density distribution of a volcanic gas, available as time-consecutive frames, provides information of a wind-field and the average velocity at which the volcanic plume is propagating. The presented reconstruction method solves the equation of continuity as an ill-posed problem using mainly a Tikhonov-like regularization. It is observed from the available data sets that if the main direction of propagation is perpendicular to the line-of-sight, the algorithm works well for SO_2 which has the strongest signals, and also for SiF_4 in some favourable cases. Due to the similarity of the algorithm used here with the reconstruction methods used for profile retrievals based on optimal estimation theory, diagnostic tools like the averaging kernels can be calculated analogously and the information can be quantified as degrees of freedom. Thus, it is shown that the combination of wind-field and column distribution of the gas plume can provide the emission flux of the volcano both during day and night.

1 Introduction

Measuring volcanic gas emissions is important for several reasons. Gas fluxes are commonly monitored by governmental agencies and research institutions for disaster prevention purposes, especially in the case of active volcanoes near cities and along major flight routes. Also, a detailed and current knowledge of the emissions of volcanoes, both eruptive and passive degassing, is important as it is well known that SO_2, for

AMTD
5, 4599–4633, 2012

example, has an indirect impact on radiative forcing and is therefore needed in climate model studies on regional and global scales (Halmer, 2002; Robock, 2000).

There is still, however, a scarce in the number of active volcanoes studied worldwide and the frequency of measurements is strongly dependent on the method used and the capacities and funding available by the responsible local institutions. Nowadays, much can be done using satellite remote sensing, but these measurements have usually large uncertainties and need continuous improvements in the quantification of gas emissions preferably through validations with ground studies. The most monitored volcanic gas is SO_2 due to its abundance and the fact that it can be readily measured using common analytical methods like DOAS (Differential Optical Absorption Spectroscopy) in the ultraviolet (UV) or FTIR (Fourier Transform Infrared Spectroscopy) in the infrared (IR), both in absorption or thermal emission modes.

Each technique and measurement geometry needs a different treatment to derive information about the emissions from the measured quantities. For example, a nadir observation from space can obtain a snapshot of the horizontal distribution of SO_2 columns and with the use of an inverse model the emission can be estimated (Kristiansen et al., 2010). Near the ground, a traverse around the volcano using scattered sunlight and the DOAS technique from various platforms gives a cross-section of the volcanic plume as a result. This can be done for example by walking (McGonigle et al., 2002), from an ultra-light aircraft (Grutter et al., 2008a) or a fixed instrument scanning the plume from below, as it is done by the NOVAC-project in a network of Multi-Axis instruments (MAX-DOAS) set up in various volcanoes around the world (Galle et al., 2010).

However, apart from the gas-column measurements, which reflects the plume cross-section, also the wind velocity has to be known to calculate emission fluxes. Normally the information is taken from ground measurements, radiosondes or reanalized meteorological data products from models. Correlations between measurements from three instruments on different locations (McGonigle, 2005), or measuring at different angles (McGonigle et al., 2005) has been done to determine the velocity. Recently, Johansson

AMTD
5, 4599–4633, 2012

et al. (2009b) developed a dual-beam device which allows the estimation of the wind velocity with a single device.

Instrumentation for imaging gas-distributions in volcanic plumes is a current topic, since it aims to provide information about the dynamics and fluxes as has been done by means of UV cameras (Bluth et al., 2007; Kantzas et al., 2010). Most scanning and imaging devices use UV radiation, however, also spectrally resolved infrared radiation has been used for characterizing the spatial distribution of industrial and volcanic emissions (Harig et al., 2005; Grutter et al., 2008b; Gross et al., 2010; Stremme et al., 2012).

In this contribution, it is shown how the propagation velocity of the gas plume can be determined from a sequence of two images and used to calculate an emission flux around the volcano. Column measurements have been retrieved from thermal infrared spectra taken with a FTIR-spectrometer at $4\,cm^{-1}$ resolution. A scanning device allowed for recording images of the slant column density of SO_2 and in some favorable cases also of SiF_4, see Part 1 (Stremme et al., 2012). Figure 1 shows an example of two sequential images with SO_2 columns in false colors from which the emission flux have been calculated. A detailed description of the methodology used for the wind-field retrieval is given in this contribution, as well as a diagnosis of the results and an analysis of the errors involved.

2 Measurements and instrumentation

The measurements were taken with a Scanning Infrared Gas Imaging System (SIGIS). It is composed of a two dimensional scanning mirror coupled to a video camera. The mirror sends the thermal radiation to a telescope and an FTIR spectrometer (OPAG 22, Bruker Daltonics, Leipzig, Germany). The instrument uses an MCT detector with a stirling-cooler and covers a spectral range from 600–5000 cm^{-1}. Its maximal spectral resolution of $0.5\,cm^{-1}$ has been used for solar absorption measurements and for thermal emission spectroscopy (Grutter et al., 2008a,b; Stremme et al., 2009, 2011).

AMTD
5, 4599–4633, 2012

However, for imaging and the analysis considered here, the spectral resolution of $4\,cm^{-1}$ is more convenient. The measurements where performed from the Altzomoni Atmospheric Observatory, which is around 12 km North of Popocatépetl at an altitude of 4000 m a.s.l. Slant columns of SO_2 and SiF_4 with an almost horizontal line-of-sight, were retrieved from the IR spectra. For more details of the instrumentation, used algorithm and realization of measurements see Part 1 of this work (Stremme et al., 2012).

3 Methodology

3.1 Basic principle

The spatial distribution provided by the column density images together with their temporal change allow for the velocity and direction of the propagating plume ($\boldsymbol{v}$) to be calculated. The approach how this information can be extracted mathematically is the main topic of this work. The density distribution and its temporal evolution is described by the equation of continuity. This applies not only for the number density (ρ) of SO_2, SiF_4 or any detectable gas with volcanic origin, but also for the slant column densities ($\boldsymbol{cl} := \int_{\mathrm{LoS}} \rho \cdot \mathrm{d}s$) measured by the instrument. The ds is the infinitesimal path along the line-of-sight (LoS) of the instrument to the top of the atmosphere, to a sight limiting cloud or to the body of the volcano.

$$\frac{\mathrm{d}}{\mathrm{d}t}\rho = -\nabla \cdot (\boldsymbol{v} \cdot \rho) + \frac{\partial}{\partial t}\rho \tag{1}$$

$$\int_{\mathrm{LoS}} \left[\frac{\mathrm{d}}{\mathrm{d}t}\rho\right] \mathrm{d}s = \int_{\mathrm{LoS}} \left[-\nabla \cdot (\boldsymbol{v} \cdot \rho) + \frac{\partial}{\partial t}\rho\right] \mathrm{d}s \tag{2}$$

A two dimensional wind field ($\boldsymbol{v}$) might be reconstructed by solving the continuity equation for the column densities of a gas with volcanic origin using Eq. (3). The left term

AMTD
5, 4599–4633, 2012

of the equation represents the change from one to the next false-color image of the observed gas column density ($\boldsymbol{cI}$) per time interval, like it is shown in Fig. 2a. $\boldsymbol{v}$ is the 2-D propagation vector and Q is the source term which describes the appearance of new gas signals in the image, being equivalent to $\int_{\mathrm{LoS}} \frac{\partial}{\partial t}\rho \cdot \mathrm{d}s$ in Eq. (2).

$$\frac{\mathrm{d}\boldsymbol{cI}}{\mathrm{d}t} = -\nabla \cdot (\boldsymbol{v} \cdot \boldsymbol{cI}) + Q. \tag{3}$$

3.2 Forward model

Equation (4) represents a linear forward model where $\mathrm{d}\boldsymbol{cI}$ is the measured quantity, $\mathbf{V}$ is the solution vector and $\mathbf{K}$ the linear forward model.

$$\mathrm{d}\boldsymbol{cI} = \mathbf{K} \cdot \mathbf{V}. \tag{4}$$

The left and right side of the equation, shown as Fig. 2a, b, represent the measured and simulated differences of the column densities between two consecutive images, respectively. As the propagation during the time between two images ($\mathrm{d}t$) might be larger than the pixel size, the images can be smoothed before $\frac{\mathrm{d}\boldsymbol{cI}}{\mathrm{d}t}$ and $\nabla\boldsymbol{cI}$ are calculated. With this not only neighbouring pixels are taken into account but the gradients might be more adequate for the finite time interval between two measurements.

The matrix $\mathbf{K}$ is rather sparse and given by the following expression:

AMTD
5, 4599–4633, 2012

$$\mathbf{K} = \mathrm{d}t \cdot \left(\mathbf{K}_x, \mathbf{K}_y, \mathbf{K}_{\mathrm{src}} \right) \tag{5}$$

$$\mathbf{K}_x = \underbrace{\begin{pmatrix} -\frac{\partial \boldsymbol{cl}_{11}}{\partial x} & 0 & \cdots & 0 \\ 0 & \ddots & \ddots & \vdots \\ \vdots & \ddots & \ddots & \vdots \\ \vdots & \ddots & \ddots & \vdots \\ \vdots & \ddots & \ddots & \vdots \\ \vdots & \ddots & \ddots & 0 \\ 0 & \cdots & 0 & -\frac{\partial \boldsymbol{cl}_{nm}}{\partial x} \end{pmatrix}}_{-\mathrm{grad}_x \boldsymbol{cl}} - \underbrace{\begin{pmatrix} \boldsymbol{cl}_{11} & 0 & \cdots & 0 & \ddots \\ 0 & \boldsymbol{cl}_{12} & \cdots & 0 & \ddots \\ \vdots & \ddots & \ddots & \vdots & \ddots \\ \vdots & \ddots & \ddots & \vdots & \ddots \\ 0 & \cdots & \cdots & \boldsymbol{cl}_{1m} & \ddots \\ \vdots & \ddots & \ddots & \ddots & \ddots \\ 0 & \cdots & \cdots & 0 & \boldsymbol{cl}_{nm} \end{pmatrix}}_{=:\boldsymbol{cl}_{\mathrm{diag}}} \underbrace{\frac{1}{\mathrm{d}x} \begin{pmatrix} -1 & 1 & 0 & \cdots & 0 & \ddots \\ -\frac{1}{2} & 0 & \frac{1}{2} & 0 & \vdots & \ddots \\ 0 & \ddots & \ddots & \ddots & 0 & \ddots \\ \vdots & \ddots & -\frac{1}{2} & 0 & \frac{1}{2} & \ddots \\ 0 & \cdots & 0 & -1 & 1 & \ddots \\ \vdots & \ddots & \ddots & \ddots & \ddots & \ddots \\ \vdots & \ddots & \ddots & \ddots & \ddots & \ddots \end{pmatrix}}_{=:\mathbf{div}_x^{mn}} \tag{6}$$

The two first expressions in $\mathbf{K}_x$ ($-\mathrm{grad}_x \boldsymbol{cl}$ and $\boldsymbol{cl}_{\mathrm{diag}}$) are diagonal matrices, but the third represents the partial derivation of x on a $m \times n$ field. The pixels are quadratic with a size of $\mathrm{d}x = \mathrm{d}y$.

The operator $\tilde{\mathbf{div}}_y^{nm}$ contains n blocks and each block consists of a $m \times m$ matrix. However, the operator for the y-component does not have the same shape, as the neighbouring pixels of the same column are not neighbours in the vector, like it is the case for the rows. We define the auxiliary quantity $\tilde{\mathbf{div}}_y^{nm}$ as similar to $\mathbf{div}_x^{mn}$, but it contains now m block-matrices, each one has the dimension $n \times n$. It would be the "$\mathbf{div}_x$"-operator if the field was transformed by a unitary transformation, which mirrors (transposes) the field on the diagonal and just represents an exchange of the x and the y dimensions. This unitary transformation (T_{kl}^{lk}), a $(n \cdot m) \times (n \cdot m)$-square matrix, just exchanges the ith ($i = (l-1) \cdot n + k$) element with the jth ($j = (k-1) \cdot m + l$) element of the vectors. Each vector represents a $(n \times m)$-field.

AMTD
5, 4599–4633, 2012

$$\mathbf{K}_y = \left(-\mathrm{grad}_y \boldsymbol{cI}\right) - \left(\boldsymbol{cI}_{\mathrm{diag}}\right) \cdot \underbrace{\left(T_{kl}^{lk\,-1} \cdot \tilde{\mathbf{div}}_y^{nm} \cdot T_{kl}^{lk}\right)}_{=:\mathbf{div}_y^{mn}\text{y-comp. of }\mathbf{div}.\text{ on } m \times n \text{ field}} \tag{7}$$

$$\mathbf{K}_{\mathrm{src}} = \begin{pmatrix} 1 & \cdots & 0 \\ \vdots & \ddots & \vdots \\ 0 & \cdots & 1 \end{pmatrix} \tag{8}$$

The Eq. (3) describes an underdetermined problem with only $n \times m$ equations, corresponding to the differences in the columns of two sequential frames $\mathrm{d}\boldsymbol{cI} = (\mathrm{dcl}_{11}, \ldots, \mathrm{dcl}_{mn})$ and the $3\times$ larger solution of the atmospheric state vector $\mathbf{V} = (v_{11}^x, \ldots, v_{mn}^x, v_{11}^y, \ldots, v_{mn}^y, Q_1, \ldots, Q_{mn})$; the wind components (v_{ij}^x, v_{ij}^y), Fig. 3, plus the strength of $q = m \times n$ sources (Q_{ij}), Fig. 7b.

3.3 Inversion

As the solution vector has a larger dimension than the measurement vector, the problem would be ill-posed even if there were no measurement errors. The ill-posed Eq. (4) is solved using a mainly Tihkonov-type smoothing constraint (Tikhonov, 1963) with the following penalty function (Eq. 9) to be minimized:

$$PF = \underbrace{(\mathrm{d}\boldsymbol{cI} - \mathbf{K}\cdot\mathbf{V})^T \mathbf{S}_{\mathrm{e}}^{-1} (\mathrm{d}\boldsymbol{cI} - \mathbf{K}\cdot\mathbf{V})}_{\text{weighted least square fit}} + \underbrace{(\mathbf{V} - \mathbf{V}_{\mathrm{a}})^T \mathbf{R}(\boldsymbol{\lambda}, \boldsymbol{\mu})(\mathbf{V} - \mathbf{V}_{\mathrm{a}})}_{\text{constraint, a priori info, model assumption}} . \tag{9}$$

$\mathbf{V} = \mathbf{V}_{\mathrm{ret}}$ is the solution which minimizes the penalty function in the Eq. (9) and contains the retrieved wind propagation vectors and the source strength in all pixels. The measurement noise or error matrix $\mathbf{S}_{\mathrm{e}}^{-1}$ should describe the precision or quality of the column measurements of each pixel. In this work the matrix $\mathbf{S}_{\mathrm{e}}^{-1}$ is chosen to be diagonal and the information for the diagonal elements is taken from the spectral fit of

AMTD
5, 4599–4633, 2012

the retrievals. The residual ($d\boldsymbol{c}\boldsymbol{I} - \mathbf{K} \cdot \mathbf{V}$) in Fig. 2c shows directly the impact of the chosen weighting and it is rather small in the plume position. The weighting is realised by the initialization of the $\mathbf{S}_e^{-1}$-matrix diagonal elements in Eq. (9) in an empirical "Ad Hoc" manner as follows. The Pearson's correlation coefficient is used as weighting and is calculated between the measured spectra (from which all fitted interference gases, offset, slope and curvature have been substructed) and a reference spectrum. The root-mean-square of the linear least-square fit is actually almost linear to (1 – the correlation coefficient). The correlation coefficient as false color image is a possible output of the used algorithm and therefore the basis for the weighting matrix. In a strict optimal-estimation approach the weighting should be given by the random error in the column difference by a sequence of two images. To evaluate the impact of the matrix $\mathbf{S}_e^{-1}$ on the retrieval, it has to be compared with the regularisation matrix $\mathbf{R}$, which is built by the sum of different symmetric block-matrices and described in Sect. 3.3.1.

The regularisation matrix

Three strategies might solve a mathematically ill-posed problem: (i) Reduction of the resolution of the solution through a smoothing constraint (Tihkonov-type regularisation), (ii) adding a priori information (Bayesian approach) and (iii) parametrization of the solution vector. The construction of the matrix $\mathbf{R}$ takes aspects of these three into account and the borders between the strategies are rather blurred in an empirically adjusted retrieval.

The first order difference operator $\mathbf{D}_1$ (also called L_1-operator in e.g. Steck, 2002; von Clarmann and Grabowski, 2007) calculates the differences between neighbouring values. $\boldsymbol{\lambda} \cdot \mathbf{D}_1^T \mathbf{D}_1$ constrains the solution towards a smoothed solution without constraining the average values of the x-,y-components of the velocities and sources. The optimal estimation strategy is realized partly and in an empirical manner by another term which constrains (with strength $\boldsymbol{\mu}$) each value of the solution vector towards an a priori value of $\mathbf{V}_a$. This constraint affects the average wind velocity of all pixels, but it allows to include in a simple manner a priori information of independent measurements or even

AMTD
5, 4599–4633, 2012

from the same data by applying a different strategy like a cross-correlation, Sect. 4.1. In the algorithm used in this work only one a priori velocity $(\boldsymbol{v}_{\mathrm{a}}^{x}, \boldsymbol{v}_{\mathrm{a}}^{y})$ valid for all pixels in the image is chosen.

Information concerning the location of sources and sinks is also needed. In the solution of Eq. (3) no limits of the area are taken into account, however, at the border of the considered area a SO_2 plume is expected to enter or leave the observed area. This should be reflected by the retrieved sources or sinks in exactly those pixels where the plume meets the border. The constraint should ensure that such a solution is not suppressed. Therefore, a term is added to free the border and all pixels which are considered as potential sources from a smoothness constraint and treat their regulation individually, Fig. 7a. The choice of location where potential sources are expected and constraining differently as background might be considered a kind of parametrisation.

$\mathbf{R} = \boldsymbol{\lambda} \cdot \mathbf{D}_1^T \mathbf{D}_1 + \boldsymbol{\mu} \cdot \mathbf{1} + \mathbf{R}_{\mathrm{src}}$ is constructed from three terms each consisting of three block-matrices. Two blocks concerning the x and y components of the wind field $(\mathbf{V}_x, \mathbf{V}_y)$ and the third the sources $(\mathbf{V}_{\mathrm{src}})$. However, as the measured column image (a 2-D distribution) is represented by a $m \times n$-vector, the difference operator for each component $(\mathbf{V}_x, \mathbf{V}_y, \mathbf{V}_{\mathrm{src}})$ concerning the vertical smoothing (columns) $\mathbf{D}_1^{\mathrm{cols}}$ does not have a block-shape if the enumeration of the pixel is so chosen that the operator concerning the (rows) $\mathbf{D}_1^{\mathrm{rows}}$ is of block-shape:

AMTD
5, 4599–4633, 2012

$$\mathbf{D}_1^{\mathrm{row}} = \underbrace{\left.\begin{pmatrix} 1 & -1 & 0 & \cdots & \cdots & 0 \\ 0 & 1 & -1 & \ddots & \ddots & \vdots \\ \vdots & \ddots & \ddots & \ddots & \ddots & \vdots \\ \vdots & \ddots & \ddots & \ddots & \ddots & 0 \\ 0 & \cdots & \cdots & \ddots & 1 & -1 \\ 0 & \cdots & \cdots & \cdots & 0 & 0 \end{pmatrix}\right\} m;}_{m-\mathrm{cols}} \quad \mathbf{D}_1^{\mathrm{rows}} = \underbrace{\left.\begin{pmatrix} \mathbf{D}_1^{\mathrm{row}_0} & 0 & 0 & 0 \\ 0 & \mathbf{D}_1^{\mathrm{row}_1} & 0 & 0 \\ 0 & 0 & \mathbf{D}_1^{\mathrm{row}_2} & 0 \\ \cdots & \cdots & \cdots & \vdots \\ 0 & 0 & 0 & \mathbf{D}_1^{\mathrm{row}_n} \end{pmatrix}\right\} n}_{n-\mathrm{rows}} \qquad (10)$$

$$\tilde{\mathbf{D}}_1^{\mathrm{col}} = \underbrace{\left.\begin{pmatrix} 1 & -1 & 0 & \cdots & \cdots & 0 \\ 0 & 1 & -1 & \ddots & \ddots & \vdots \\ \vdots & \ddots & \ddots & \ddots & \ddots & \vdots \\ \vdots & \ddots & \ddots & \ddots & \ddots & 0 \\ 0 & \cdots & \cdots & \ddots & 1 & -1 \\ 0 & \cdots & \cdots & \cdots & 0 & 0 \end{pmatrix}\right\} n;}_{n-\mathrm{rows}} \quad \tilde{\mathbf{D}}_1^{\mathrm{cols}} = \underbrace{\left.\begin{pmatrix} \tilde{\mathbf{D}}_1^{\mathrm{col}_0} & 0 & 0 & 0 \\ 0 & \tilde{\mathbf{D}}_1^{\mathrm{col}_1} & 0 & 0 \\ 0 & 0 & \tilde{\mathbf{D}}_1^{\mathrm{col}_2} & 0 \\ \cdots & \cdots & \cdots & \vdots \\ 0 & 0 & 0 & \tilde{\mathbf{D}}_1^{\mathrm{col}_m} \end{pmatrix}\right\} m.}_{m-\mathrm{cols}} \qquad (11)$$

The difference operators $\tilde{\mathbf{D}}_1^{\mathrm{cols}}$ in Eq. (11) has a block-matrix shape, but is not described in the same vector space in which $\mathbf{D}_1^{\mathrm{rows}}$ is described. That is why the mapping of the 2-D distribution (field of velocity components and sources) to a vector space for $\mathbf{D}_1^{\mathrm{rows}}$ is done by taking the 1st-row first and then the 2nd row of the field ... but $\tilde{\mathbf{D}}_1^{\mathrm{cols}}$ is designed for a vector which contains the 1st-column first and then goes on with the 2nd-column of the field. It is therefore mapped in the same vector-space in which $\mathbf{D}_1^{\mathrm{rows}}$ operates. This is realized by the unitary transformation T_{kl}^{lk} already used earlier for the divergence-operator.

AMTD
5, 4599–4633, 2012

$$\mathbf{D}_1^{\text{cols}} = (T_{kl}^{lk})^{-1}\tilde{\mathbf{D}}_1^{\text{cols}}T_{kl}^{lk} \tag{12}$$

$$\mathbf{D}_1 = \mathbf{D}_1^{\text{rows}} + \mathbf{D}_1^{\text{cols}} \tag{13}$$

$$\mathbf{R} = \underbrace{\begin{pmatrix} \lambda_x \cdot \mathbf{D}_1{}^T\mathbf{D}_1 & 0 & 0 \\ 0 & \lambda_y \cdot \mathbf{D}_1{}^T\mathbf{D}_1 & 0 \\ 0 & 0 & \lambda_{\text{src}} \cdot \mathbf{D}_1{}^T\mathbf{D}_1 \end{pmatrix}}_{\text{smoothing constraint}} + \underbrace{\begin{pmatrix} \mu_x \cdot 1 & 0 & 0 \\ 0 & \mu_y \cdot 1 & 0 \\ 0 & 0 & \mu_{\text{src}} \cdot 1 \end{pmatrix}}_{\text{constraint towards a priori}} + \underbrace{\begin{pmatrix} 0\,0 & 0 \\ 0\,0 & 0 \\ 0\,0 & \mathbf{R}_{\text{src}} \end{pmatrix}}_{\text{sources}}. \tag{14}$$

The first term of **R** is a smoothing constraint which encourages the neighbouring wind velocity components and sources in **V** to have similar size and therefore the wind vectors to point in the same direction. The strength of the constraint for the wind-field is given by λ_x, λ_y, which are chosen to have the same strength. The strength of the field of sources λ_{src} is independently chosen but has the same smoothing effect.

The second term constrains the solution towards the a priori. This constraint is first turned off ($\mu_x = \mu_y = 0$) for the wind velocity components, but it offers the possibility to include other information about the wind velocities taken from a cross-correlation (as in the example shown in this work), from the average of prior retrieved velocities or also from independent measurements e.g. from radiosondes. The sources are normally constrained towards zero.

The third term of the constraint refers to the sources only. The matrix $\mathbf{R}_{\text{src}}$ is automatically initialized using the information where sources or sinks are expected. The whole frame is a potential source or sink as the SO_2 plume can enter or leave the image. The same argument applies for the body and crater of the volcano and opaque clouds. Both can be identified from the recorded spectra as the observed intensity in the mid-infrared is much higher in these pixel. For these pixels the constraint in terms 1 and 2 will be eliminated and just a very small value is added to the diagonal to ensure that the problem can be solved mathematically.

AMTD
5, 4599–4633, 2012

4 Diagnostics and errors

Independently of how the wind velocities are calculated, three problems might arise if conditions are not favourable, (a) the wind speed is too fast for the frame rate and size of the recorded imagines, (b) there is a repetitive pattern with more similar maxima or minima, so that the algorithm might not distinguish them and (c) there might not be sufficient structure in the images.

For case (a) the wind-speed range is limited and thus this criterion should be taken into account when choosing the frame rate while measuring, as frames need to be refreshed soon enough to capture the wind propagation features. However, if more puffs are available in the images (case b) so that the propagation of the puffs are ambiguous, different approaches could be tried:

First, an adequate smoothing might eliminate smaller minima and maxima which would allow the main structure to remain. If, however, a new puff appears near the crater with a similar magnitude in its anomaly as the one already in the image, the stronger smoothing might not work. In this cases a wind velocity might be obtained which would point in the wrong direction. Since such an event might appear just once in a while most pair of images lead to a correct velocity, an iterative analysis of the time series or Kalmann-filter might be used to eliminate results and improve the wind speed retrieval in the time series.

In the case (c), which describes the situation where there might be no sufficient structure in the plume to retrieve a wind velocity field, there is still a chance to reconstruct a mean velocity which includes the main direction and speed of propagation. This result can be later checked or improved by a cross-correlation (Sect. 4.1) and how much information about the wind velocity field is extracted in a retrieval is described in Sect. 4.2.

AMTD
5, 4599–4633, 2012

4.1 Cross-correlation

The method presented in the previous sections is different as the approach using only cross-correlations (Johansson et al., 2009b; McGonigle et al., 2005) to obtain a propagation vector. However, it allows for the uses of cross-correlation as correction and check of the retrieved wind speed. Following is the scheme used for the results shown in Fig. 4 which serves to improve the wind speed retrieval.

First, the time series of the wind-fields are retrieved using a pure smoothing constraint and the spatially average wind velocities are calculated (for the average the wind is weighted by the SO_2 column). Typically the direction is well retrieved but the absolute wind speed might be off. After the direction is retrieved, the upper boundary of wind speed is constrained to a moderate value of $2\,\mathrm{m\,s^{-1}}$ and a new wind-field is obtained (arrows like in Fig. 3)[1].

The SO_2 flow column density ($\boldsymbol{j}$) is calculated by multiplying the wind-field with the SO_2 column densities in each pixel.

$$\boldsymbol{j}_{ij}^{\text{former}} = \boldsymbol{cl}_{ij}^{\text{former}} \cdot \boldsymbol{v}_{ij} \qquad \boldsymbol{j}_{ij}^{\text{latter}} = \boldsymbol{cl}_{ij}^{\text{latter}} \cdot \boldsymbol{v}_{ij}. \tag{15}$$

Below is the same equation but in other coordinates, k is along the trajectory and s is perpendicular to it.

$$\boldsymbol{j}_{s_k}^{\text{former}} = \boldsymbol{cl}_{s_k}^{\text{former}} \cdot \boldsymbol{v}_{s_k} \qquad \boldsymbol{j}_{s_k}^{\text{latter}} = \boldsymbol{cl}_{s_k}^{\text{latter}} \cdot \boldsymbol{v}_{s_k}. \tag{16}$$

A time series of the emission fluxes at different distances from the crater results from integrating the flux densities perpendicular to the linear approximated trajectory (near-horizontal line in Fig. 3) separately for the two false color images (former and latter).

[1] This strategy aims to obtain a reliable spacing in time for the next step (the distances of the black lines in Fig. 3 indicate the spacing). The chosen value of $2\,\mathrm{m\,s^{-1}}$ has no influence in the final result.

AMTD
5, 4599–4633, 2012

$$E_k^{\text{former}} = \int_{C_k} < \hat{\boldsymbol{n}} \cdot \boldsymbol{j}_{s_k}^{\text{former}} > \cdot \mathrm{d}s_k \qquad E_k^{\text{latter}} = \int_{C_k} < \hat{\boldsymbol{n}} \cdot \boldsymbol{j}_{s_k}^{\text{latter}} > \cdot \mathrm{d}s_k. \tag{17}$$

$\hat{\boldsymbol{n}}$ is a normalised vector with direction of the direction of the propagation of the plume and $\mathrm{d}s_k$ is a small part of the cross-section (C_k) which is perpendicular to $\hat{\boldsymbol{n}}$ and has the distance to the crater d_k. The location of the crater is the beginning of the linear track (black straight line in Fig. 3). The corresponding time t_k is obtained from the distance d_k and the averaged wind speed $|\boldsymbol{v}_{\text{ret}}|$ between the center of the source (crater), the estimated location of the crater and the beginning of the linear trajectory, and the averaged wind speed $|\boldsymbol{v}_{\text{ret}}|$.

$$t_k = \frac{d_k}{|\bar{\boldsymbol{v}}_{\text{ret}}|}. \tag{18}$$

The two slightly different time series are compared in Fig. 4. One uses the column density from the first frame measured and the second uses the second which is needed for the wind-field calculation. For testing the calculated wind-fields, the time series are cross-correlated (Fig. 5) and the resulting time shift (t_{shift}) should match the time difference between the measurements (t_{frames}), as it is shown in Fig. 5. If these times are not equal, a scaling factor for the wind speeds is calculated and used for the calculation of the a priori information ($\boldsymbol{v}_{\text{a}}$) in the final (third) retrieval.

$$\boldsymbol{v}_{\text{a}} = \frac{t_{\text{shift}}}{t_{\text{frames}}} \cdot \boldsymbol{v}_{\text{ret}}. \tag{19}$$

There are different possibilities in calculating the time series of the emission fluxes, either by assuming a constant wind speed which leads to a constant spacing of the cross-sections (the black lines in Fig. 3 perpendicular to the propagation), or to use the individual wind speeds projected to the main wind direction with variable spacings of

AMTD
5, 4599–4633, 2012

the cross-sections. There is a trade-off between an individually adopted flux calculation and an algorithm applying for various measurements, thus we try to keep the calculation of the flux-time series simple. It should be mentioned that cross-sections and main plume propagation does not have to be approximated by straight lines, as it is done in this work. A variable spacing is in favour of a correct emission flux and could lead to a much higher correlation. However, if the retrieved spacing is wrong the result of the cross-correlation will also be wrong. An effort to improve the correlation by a more sophisticated flux calculation might only be realized with an iterative approach.

The following problem might arise and has to be solved before a cross-correlation is calculated: the two time series in Fig. 4 should not show a correlation at the borders because in the prior image some of the SO_2 near the body of the volcano has not yet been emitted and in the latter image some of the SO_2-plume has already left the image. However, for geometrical and others important reasons (dispersion, cooling and chemical transformations, etc.) there is a modification of the emission fluxes which depends on where in the image the emission flux is calculated. This effect is strong where the plume touches the borders of the image, so that a part of the SO_2 is missing and the calculated emission flux is under estimated. To avoid this geometrical effect, only the middle of the plot in Fig. 4 is taken into account. The diminishing effects of the plume with time or distance from the crater is compensated by fitting a straight line to each of the emission flux time series and subtracting it afterwards. These corrected time series are used as cross-correlation checks as in Fig. 5.

The decreasing of the retrieved SO_2 amount and the emission flux with time might originate from different effects: (a) Cooling of the plume: If the true temperature is cooler than the temperature assumed in the retrieval, the retrieved column will be smaller than the true column of SO_2. The cooling might also lead to a faster condensation of the gas into the liquid phase and decreases additionally the true column of SO_2 gas. (b) Chemical transformation or dispersion might decrease the true (and therefore also the retrieved) column of SO_2. (c) The retrieved wind velocities are constrained and might slightly overestimate the propagation speed of the SO_2 freshly released near the crater

AMTD
5, 4599–4633, 2012

and underestimate the wind speed at larger distances. Through such a systematic error the calculated emission flux would decrease with time.

4.2 Averaging kernel and resolution

The information obtained from the analysis depends on the trace gas and if the velocity is somehow perpendicular to the line-of-sight. Therefore, the conditions can be more or less favourable for the wind field retrieval. The averaging kernel (**AK**), also called the data resolution matrix, is a useful diagnostic tool to track the origin of the information in a constrained retrieval. It can also be used to quantify the information in the retrieval.

$$\mathbf{AK}_{kl}^{ij} = \frac{\partial V^{\mathrm{ret}} ij}{\partial V_{kl}^{\mathrm{true}}} \underbrace{=}_{\text{retrieval based on OET/Tihkonov...}} (\mathbf{K}^T \mathbf{S}_e^{-1} \mathbf{K} + \mathbf{R})^{-1} \mathbf{K}^T \mathbf{S}_e^{-1} \mathbf{K}. \quad (20)$$

(ij) and (kl) are indices with values from 1 to $(3 \times n \times m)$. The **AK** does not have a block-matrix form, but here just the 3 blocks concerning the x and y-components of the velocities and the source strength of the pixels are considered separately. Further, we limit our discussion to the diagonal of the **AK** so that we might address the diagonal elements of the averaging kernel of the pixel i,j as $\mathbf{AK}_x^{ij}$,$\mathbf{AK}_y^{ij}$ and $\mathbf{AK}_{\mathrm{src}}^{ij}$ in an intuitive way.

The diagonal of the **AK** reflects the sensitivity of the retrieval (Funke et al., 2009). The sum of the diagonal, trace(**AK**), is the degree of freedom (DOF) of the signal (Rodgers, 2000) and its value shows how many independent quantities are retrieved. DOF, calculated separately for the blocks of the x, y-components of the velocity and the source strength, show that the information is not dispersed homogeneously over the three blocks. The DOF_x, DOF_y and $\mathrm{DOF}_{\mathrm{src}}$ are independent quantities and have the values 68.6, 92.7, and 11.7, respectively. Different values are expected for the sources as they have a different character and are differently constrained. However, a difference between the DOF regarding to the $\boldsymbol{v}_x$ and $\boldsymbol{v}_y$ components is of outermost importance. It might explain why the retrieval works well for the calculation of the wind direction,

AMTD
5, 4599–4633, 2012

although in some observed cases there are difficulties for the proper determination of the wind speeds.

The forward model **K** consists mainly of the gradient of the column densities and especially in the case of a continuous emission, this gradient is strong perpendicular to the propagation and small or even not significant in its direction. In the example shown in Fig. 3, the main direction of propagation is in the direction of x and explains the imbalance in the calculated DOFs for the $\mathbf{V}_x$ and $\mathbf{V}_y$ components.

In general, even if the main propagation direction does not coincide with one of the axes, it might be possible to rotate the image by a unitary transformation and to calculate two blocks of the averaging kernels, $\mathbf{AK}_{e_r}$ as the parallel and $\mathbf{AK}_{e_\phi}$ the perpendicular wind component, respectively, to the main direction in which the plume is propagating. With this in mind, the discussion of the presented example can transferred to all other cases. $\mathbf{AK}_{e_\phi}$ (here $\mathbf{AK}_y$) depends more or less on the amount of gas in the image, because the gradient at the edge of the plume and the matrix $\mathbf{K}_y$ scales with it. $\mathbf{AK}_{e_r}$, here $\mathbf{AK}_x$ in Fig. 6a), depends however on the structures in the emission flux (the modulation of the gas plume). The information in the retrieval concerning $\mathbf{AK}_{e_r}$ is slightly smaller if the gas is emitted continuously and there is only a small gradient of column density in the direction of the plume. The cross-correlation described in the Sect. 4.1 is useful in such cases since a reliable mean velocity can be calculated and used as a priori in the subsequent retrieval.

The averaging kernel regarding the source strength retrieval is different. In the free atmosphere this term might just help to improve the fit as no sources are expected for SO_2. However, where the plume leaves the image a strong sink should be retrieved. The diagonal of the averaging kernel regarding the sources is shown in Fig. 6c and reflects that the retrieval is sensitive in the pixel where the $\mathbf{S}_e^{-1}$ allows to take information from the images and for which the sources are not constrained by the regularisation **R**. Both conditions are met where the plume leaves the image.

The used regularisation regarding the strength of the sources in each pixel is visualized as the corresponding part of the diagonal of the matrix **R** in Fig. 7a. This figure

AMTD
5, 4599–4633, 2012

illustrates how the information about the body of the volcano, taken from the same frame of spectra, is used in the inversion.

4.3 The dispersion of source strength

The retrieved dispersion of source strength in Fig. 7b is part of the retrieved vector. In Fig. 7b the source dispersion shows an maximum above the crater and a strong sink, where the plume leaves the image. The averaging kernel diagonal, Fig. 6c, shows sensitivity of the retrieval in this pixel where the sink is retrieved. The maximum of the source strength above the crater is in a region where the sources are constraint by a smoothing constraint and therefore smoothed out. The location of the source is the beginning of the plume and consistent with the implemented forward model. The constraint suppresses solutions where the direction of propagation changes strongly. Therefore the retrieved solution does not show that the SO_2 leaves the crater, but finds that a source above the crater is releasing SO_2. The retrieved sources along the plume decrease, which might reflects that the velocity of the SO_2 molecules along the plume increases, what means that near the crater the true velocity is overestimated and near the right border it is underestimated. This might result from the regularisation of the velocity towards a mean velocity.

4.4 Errors of the emission flux

Analogously to atmospheric profile retrievals and according to Rodgers (2000), three different kind of errors should be discussed: (a) the forward-model errors (b) the measurement-noise error (random error) and (c) the smoothing error which mainly describes the effect of the constraint.

4.4.1 Forward-model error

The error in the emission flux can either originate from the column retrieval of the target gas or from the determination of the velocity and size of the plume. The errors

AMTD
5, 4599–4633, 2012

affecting the column retrievals are in the radiometric calibration and the uncertainty in the estimation of the plume temperature. Both are already discussed in detail in Part 1, where the resulting error in the column densities were estimated to be around 20 %.

Important to consider here is a geometrical error, which arises from the uncertainty in the distance between the observation site and the plume. The error ($\delta r = r_{\text{esitmated}} - r_{\text{true}}$) in the estimation of the distance r affects the estimation of the amount of a gas cloud by $(\delta r/r)^2$ (see Part 1). Equally, the movement of the gas cloud can be erroneously calculated if the estimated difference r is wrong. In fact, only the velocity of the viewing angle $\frac{d\phi}{dt}$ can be obtained from measurement (Fig. 5) and has to be multiplied by an estimated distance r.

The apparent velocity results to be different from the true plume velocity and the difference is given by $\frac{d\phi}{dt} \cdot \delta r$. The uncertainty of the emission flux thus depends quadratically $(\delta r/r)^2$ on the uncertainty in the instrument-plume distance r. A 10 % overestimation of r ($\delta r \approx +1$ km) results in an overestimation of the emission flux of around 21 %.

4.4.2 Measurement-noise error

Here both the input vector d$\boldsymbol{cl}$ but also the **K**-matrix, which contains the gradient of the measured $\boldsymbol{cl}$, are affected by the measurement noise (the random errors in the retrieved columns). Also the random errors of the columns and their difference (latter-former) in the individual pixels are not completely independent in each image. Therefore, no easy estimation of the measurement noise matrix is possible. There is a difference if the error of the averaged velocity or the error of the retrieved velocity of one of the pixels is considered. The error of the average velocity is normally smaller than that of the velocity in a single pixel. In this work, no measurement error can be calculated, but if a continuous monitoring program would be implemented, more insight of how the time series are changing and to which part the solution varies randomly from measurement to measurement would be obtained.

AMTD
5, 4599–4633, 2012

4.4.3 Smoothing error

As an averaging kernel **AK** is calculated in Sect. 4.2, a "general" smoothing error **SM** could be calculated,

$$\mathbf{SM} = (\mathbf{AK} - \mathbf{1})^T \mathbf{S}_a (\mathbf{AK} - \mathbf{1}) \quad (21)$$

if (i) the a priori covariance of the wind field and source distribution $\mathbf{S}_a$ would be known and (ii) the averaging kernel would be constant. However, no $\mathbf{S}_a$ is known and the **AK** is variable so that the discussion is limited to qualitative aspects and how the smoothing error affects the retrieved wind direction and speed, Eq. (22).

$$\epsilon_{SM} = (\mathbf{AK} - \mathbf{1})(\mathbf{V}_{\text{true}} - \mathbf{V}_a) \quad (22)$$

It is clear that the wind field in the Fig. 8a, b is constrained and that a true velocity field would show a change in the direction with altitude above the crater. The effect of a constrained wind field is visible in Fig. 4, as the wind speed near the crater is overestimated while near the border seems to be underestimated. Such a solution results in less gas near the crater and more gas near the borders, if this residual would not be compensated by the field of sources like shown in Fig. 7b.

The smoothing errors on the emission-flux times series calculation could be calculated using Eqs. (22), (16) and (17), if the $\mathbf{V}_{\text{true}}$ could be estimated.

5 Results and discussion

5.1 Velocity retrieval from different trace gases: SiF_4 versus SO_2

A wind field retrieval has already been shown in Fig. 3 from SO_2 columns measured during passive degassing periods of the volcano. When another gas can be detected, like SiF_4 during an eruptive event on 18 November 2008 (see Part 1), an independent

AMTD
5, 4599–4633, 2012

wind field retrieval can be performed and compared, like is shown in Fig. 8a and b. The retrieved wind speeds perpendicular to the line-of-sight from SiF_4 and SO_2 were found to be 0.8 $m\,s^{-1}$ and 0.7 $m\,s^{-1}$, respectively.

As the SiF_4-column retrievals have large random errors the velocity retrieval is rather strong constrained and only the average velocity was determined. However, the form of the SiF_4-plume and the propagation determined is confirmed using the SO_2-plume as tracer, indicating that the volcanic gases first rise and then drift to the East (left from the image). The horizontal velocity is rather small, and the initial ascent of the gas is visible. Unfortunately, the wind-direction close to the source is not perpendicular since the velocities are strongly constrained towards a mean average velocity.

5.2 SO_2 emission flux

The estimated emission flux in the night of 1 to 2 December 2008 (22:43 LT), shown in Figs. 3 and 4, is found to be around 1000 $t\,d^{-1}$ (with a maximal value of 1200 $t\,d^{-1}$). The result of this "snapshot" is a typical value for the Popocatépetl and only slightly smaller than the average emission rates found in the literature. SO_2 emission of Popocatépetl has been estimated for different times and periods. An average emission rate of 2000–3000 $t\,d^{-1}$ is reported by Delgado-Granados et al. (2001) for the pre-eruptive phase and an average with standard deviation of (2450 ± 1390) t of daily SO_2 emission was found by Grutter et al. (2008a) during an intensive measurement campaign in March of 2006. The average of the daily SO_2 emission during a two year period (2005–2007) was calculated by the NOVAC-project and found to be 1503 $t\,d^{-1}$ with a standard deviation of 1154 $t\,d^{-1}$ (Rivera, 2009).

The reconstructed wind velocity can be compared with the velocity measured by the radiosondes which ascent at 06:00 a.m. LT near the airport. The radiosonde reports a wind speed of 2.1 $m\,s^{-1}$ and a wind direction of 69° N in the altitude 5450 m.a.s.l. As Altzomoni is located at 343° to the North of the crater, an exact perpendicular wind direction would be 73° which is almost given by the radiosonde measurements. This

AMTD
5, 4599–4633, 2012

is a necessary condition to compare wind speeds directly, otherwise the wind velocity has to be projected to the perpendicular plane. The mean wind speeds retrieved with this experiment (2.0 $m\,s^{-1}$) is consistent with the radiosonde measurement.

6 Conclusions

This work presents a method for estimating the propagation of a volcanic plume from measured thermal IR gas columns by constructing a 2 dimensional wind field. The reconstruction is based on the equation of continuity and uses a pair of sequential 2-D distributions of the column densities. The column densities are provided by a scanning infrared gas imaging spectrometer, as described in Part 1, but the algorithm can be applied to other imaging devices as well. The wind vectors can be displayed on-line over the gas-distribution sequences as an animation (see Supplement), and the overall propagation velocity serves to calculate emission gas fluxes from the volcano.

The reconstruction method uses optimal estimation and a Tihkonov-like regularisation, allowing for the definition, calculation and the use of averaging kernels in analogy to atmospheric profile retrievals. The algorithm has been tested on volcanic plumes measured on several occasions during the 2007–2009 period from Popocatépetl in Central Mexico. Plume propagation velocities retrieved independently from SiF_4 and SO_2 were presented in one example and found to be self consistent.

It is shown that at favorable conditions, the average velocity from SO_2 column densities could be retrieved with this algorithm and confirmed by an independent cross-correlation method and from radiosonde data. In one example the calculated SO_2 emission flux of 1000 $t\,d^{-1}$ is a reliable result and consistent with the current knowledge of Popocatépetl's emission fluxes and variability. This methodology complements other techniques like the mobile and scanning DOAS instruments, but adds on the possibility of monitoring also during the night and with an entirely different approach. A longer time series would be desired in order to allow for cross-validation of the calculated emission fluxes and compare with other methods.

AMTD
5, 4599–4633, 2012

Acknowledgement. We thank both anonymous referees for their helpful and motivating comments. Claudia Rivera assisted with important discussions, Ivan Ortega helped with the measurements and Alfredo Rodriguez form the workshop provided us with technical support. We are also grateful with CONANP (the Izta-Popo National Park authorities) for their support and hosting the Altzomoni Atmospheric Observatory. DGAPA-UNAM (IA101112) is acknowledged for funding this work.

Supplementary material related to this article is available online at: http://www.atmos-meas-tech-discuss.net/5/4599/2012/amtd-5-4599-2012-supplement.zip.

References

Bluth, G. J. S., Shannon, J. M., Watson, I. M., Prata, A. J., and Realmuto, V. J.: Development of an ultra-violet digital camera for volcanic SO_2 imaging, J. Volcanol. Geoth. Res., 161, 47–56, http://linkinghub.elsevier.com/retrieve/pii/S0377027306003957 (last access: 29 June 2012), 2007. 4602

Delgado-Granados, H., González, L. C., and Sánchez, N. P.: Sulfur dioxide emissions from Popocatépetl volcano (Mexico): case study of a high-emission rate, passively degassing erupting volcano, J. Volcanol. Geoth. Res., 108, 107–120, doi:10.1016/S0377-0273(00)00280-8, 2001. 4620

Funke, B., López-Puertas, M., García-Comas, M., Stiller, G. P., von Clarmann, T., Höpfner, M., Glatthor, N., Grabowski, U., Kellmann, S., and Linden, A.: Carbon monoxide distributions from the upper troposphere to the mesosphere inferred from 4.7 µm non-local thermal equilibrium emissions measured by MIPAS on Envisat, Atmos. Chem. Phys., 9, 2387–2411, doi:10.5194/acp-9-2387-2009, 2009. 4615

Galle, B., Johansson, M., Rivera, C., Zhang, Y., Kihlman, M., Kern, C., Lehmann, T., Platt, U., Arellano, S., and Hidalgo, S.: Network for Observation of Volcanic and Atmospheric Change (NOVAC) – a global network for volcanic gas monitoring: Network layout and instrument description, J. Geophys. Res.-Atmos., 115, D05304, doi:10.1029/2009JD011823, 2010. 4601

AMTD
5, 4599–4633, 2012

Gross, K. C., Bradley, K. C., and Perram, G. P.: Remote identification and quantification of industrial smokestack effluents via imaging Fourier-transform spectroscopy, Environ. Sci. Technol., 44, 9390–9397, doi:10.1021/es101823z, 2010. 4602

Grutter, M., Basaldud, R., Rivera, C., Harig, R., Junkerman, W., Caetano, E., and Delgado-Granados, H.: SO_2 emissions from Popocatépetl volcano: emission rates and plume imaging using optical remote sensing techniques, Atmos. Chem. Phys., 8, 6655–6663, doi:10.5194/acp-8-6655-2008, 2008a. 4601, 4602, 4620

Grutter, M., Basaldud, R., and Harig, R.: Optical remote sensing for characterizing the spatial distribution of stack emissions, in: Advanced Environmental Monitoring, edited by: Kim, Y. J. and Platt, U., ISBN: 978-1-4020-6363-3, Springer Verlag GmbH, 2008b. 4602

Halmer, M.: The annual volcanic gas input into the atmosphere, in particular into the stratosphere: a global data set for the past 100 years, J. Volcanol. Geoth. Res., 115, 511–528, doi:10.1016/S0377-0273(01)00318-3, 2002. 4601

Harig, R., Rusch, P., Dyer, C., Jones, A., Moseley, R., and Truscott, B.: Remote measurement of highly toxic vapors by scanning imaging Fourier-transform spectrometry, Proc. SPIE, 5995, 599510 doi:10.1117/12.631730, 2005. 4602

Johansson, M., Galle, B., Rivera, C., and Zhang, Y.: Tomographic reconstruction of gas plumes using scanning DOAS, B. Volcanol., 71, 1169–1178, doi:10.1007/s00445-009-0292-8, 2009a.

Johansson, M., Galle, B., Zhang, Y., Rivera, C., Chen, D., and Wyser, K.: The dual-beam mini-DOAS technique-measurements of volcanic gas emission, plume height and plume speed with a single instrument, B. Volcanol., 71, 747–751, doi:10.1007/s00445-008-0260-8, 2009b. 4601, 4612

Kantzas, E. P., McGonigle, A. J. S., Tamburello, G., Aiuppa, A., and Bryant, R. G.: Protocols for UV camera volcanic SO_2 measurements, J. Volcanol. Geoth. Res., 194, 55–60, http://linkinghub.elsevier.com/retrieve/pii/S0377027310001447 (last access: 29 June 2012), 2010. 4602

Kazahaya, R., Mori, T., Kazahaya, K., and Hirabayashi, J.-I.: Computed tomography reconstruction of SO_2 concentration distribution in the volcanic plume of Miyakejima, Japan, by airborne traverse technique using three UV spectrometers, Geophys. Res. Lett., 35, 2–7, http://www.agu.org/pubs/crossref/2008/2008GL034177.shtml (last access: 29 June 2012), 2008.

AMTD
5, 4599–4633, 2012

Kristiansen, N. I., Stohl, A., Prata, A. J., Richter, A., Eckhardt, S., Seibert, P., Hoffmann, A., Ritter, C., Bitar, L., Duck, T. J., and Stebel, K.: Remote sensing and inverse transport modeling of the Kasatochi eruption sulfur dioxide cloud, J. Geophys. Res.-Atmos., 115, D00L16, doi:10.1029/2009JD013286, 2010. 4601

McGonigle, A. J. S.: Volcano remote sensing with ground-based spectroscopy, Philos T. Roy. Soc. Lond. A, 363, 2915–2929, doi:10.1098/rsta.2005.1668, 2005. 4601

McGonigle, A. J. S., Oppenheimer, C., Galle, B., Mather, T. A., and Pyle, D. M.: Walking traverse and scanning DOAS measurements of volcanic gas emission rates, Geophys. Res. Lett., 29, 1985, doi:10.1029/2002GL015827, 2002. 4601

McGonigle, A. J. S., Inguaggiato, S., Aiuppa, A., Hayes, A. R., and Oppenheimer, C.: Accurate measurement of volcanic SO_2 flux: determination of plume transport speed and integrated SO_2 concentration with a single device, Geochem. Geophy. Geosy., 6, Q02003, doi:10.1029/2004GC000845, 2005. 4601, 4612

Rivera, C.: Application of passive DOAS using scattered sunlight for quantification of gas emissions from anthropogenic and volcanic sources, Ph. D. thesis, Department of Radio and Space Science, Chalmers University of Technology, Sweden, available at: http://books.google.com.mx/books?id=Sv2jXwAACAAJ (last access: 29 June 2012), 2009. 4620

Robock, A.: Volcanic eruptions and climate, Rev. Geophys., 38, 191–220, doi:10.1029/1998RG000054, 2000. 4601

Rodgers, C. D.: Inverse methods for atmospheric sounding: theory and practice, Ser. Atmos. Oceanic Planet. Phys., 2, World Sci., Hackensack, N. J., 2000. 4615, 4617

Rusch, P. and Harig, R.: 3-D Reconstruction of gas clouds by scanning imaging IR spectroscopy and tomography, IEEE Sens. J., 10, 599–602, 2010.

Steck, T.: Methods for determining regularization for atmospheric retrieval problems, Appl. Optics, 41, 1788–1797, 2002. 4607

Stremme, W., Ortega, I., and Grutter, M.: Using ground-based solar and lunar infrared spectroscopy to study the diurnal trend of carbon monoxide in the Mexico City boundary layer, Atmos. Chem. Phys., 9, 8061–8078, doi:10.5194/acp-9-8061-2009, 2009. 4602

Stremme, W., Ortega, I., Siebe, C., and Grutter, M.: Gas composition of Popocatépetl Volcano between 2007 and 2008: FTIR spectroscopic measurements of an explosive event and during quiescent degassing, Earth Planet. Sc. Lett., 301, 502–510, doi:10.1016/j.epsl.2010.11.032, 2011. 4602

AMTD
5, 4599–4633, 2012

Stremme, W., Krueger, A., Harig, R., and Grutter, M.: Volcanic SO_2 and SiF_4 visualization using 2-D thermal emission spectroscopy – Part 1: Slant-columns and their ratios, Atmos. Meas. Tech., 5, 275–288, doi:10.5194/amt-5-275-2012, 2012. 4600, 4602, 4603

Tikhonov, V. I.: Reviews of topical problems: peaks of random processes, Sov. Phys. Uspekhi, 5, 594–611, doi:10.1070/PU1963v005n04ABEH003439, 1963. 4606

von Clarmann, T. and Grabowski, U.: Elimination of hidden a priori information from remotely sensed profile data, Atmos. Chem. Phys., 7, 397–408, doi:10.5194/acp-7-397-2007, 2007. 4607

Wright, T. E., Burton, M., Pyle, D. M., and Caltabiano, T.: Scanning tomography of SO_2 distribution in a volcanic gas plume, Geophys. Res. Lett., 35, L17811, doi:10.1029/2008GL034640, 2008.

AMTD
5, 4599–4633, 2012

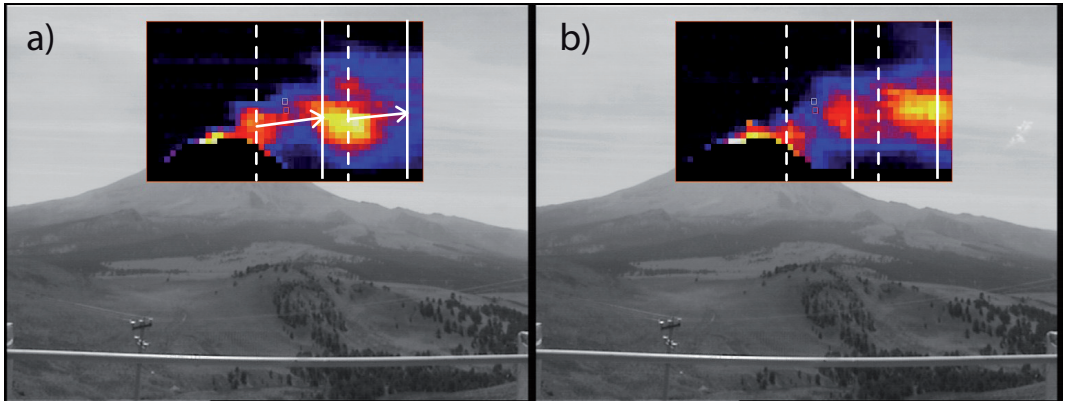

Fig. 1. A sequence of two consecutive column SO_2 images taken 3 min apart by thermal emission spectroscopy on 17 March 2006. The dash lines depict the origins of two puffs within the plume detected in frame **(a)** which has moved to the solid lines in frame **(b)**. The average wind vectors (arrows) are sought.

AMTD
5, 4599–4633, 2012

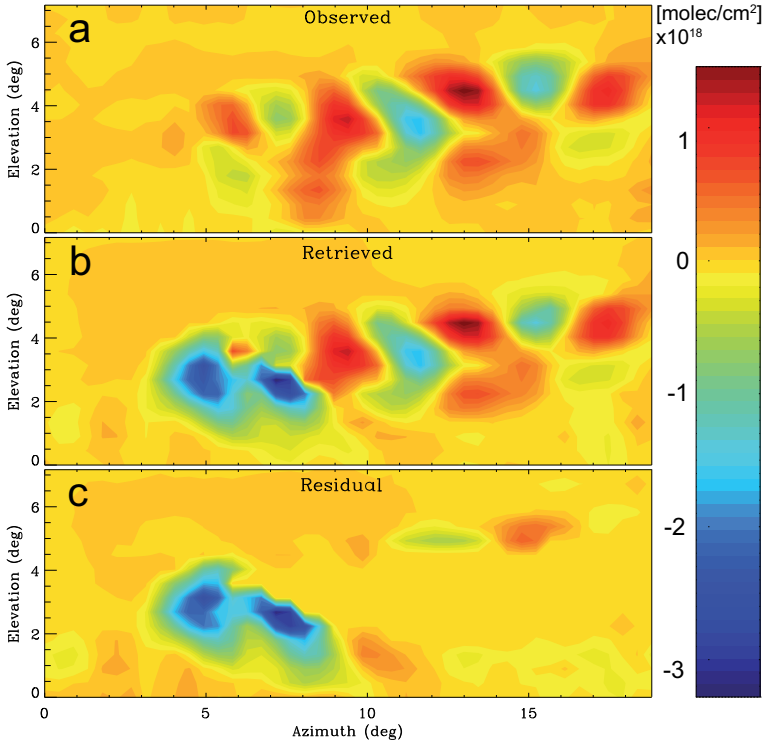

Fig. 2. False-color plot showing the difference of **(a)** the observed column distribution between two consecutive frames, representing the measured input vector for the reconstruction of the wind-field. **(b)** is the same as **(a)** but calculated using the forward model **K** and the solution vector **V**, consisting of the retrieved vector field and the retrieved source filed. The residual **(c)** is the difference between the plots above (observed – retrieved) and is almost zero at the plume position as the algorithm weights the fit with $\mathbf{S}_e^{-1}$.

AMTD
5, 4599–4633, 2012

Thermal emission spectroscopy of volcanic gases

A. Krueger et al.

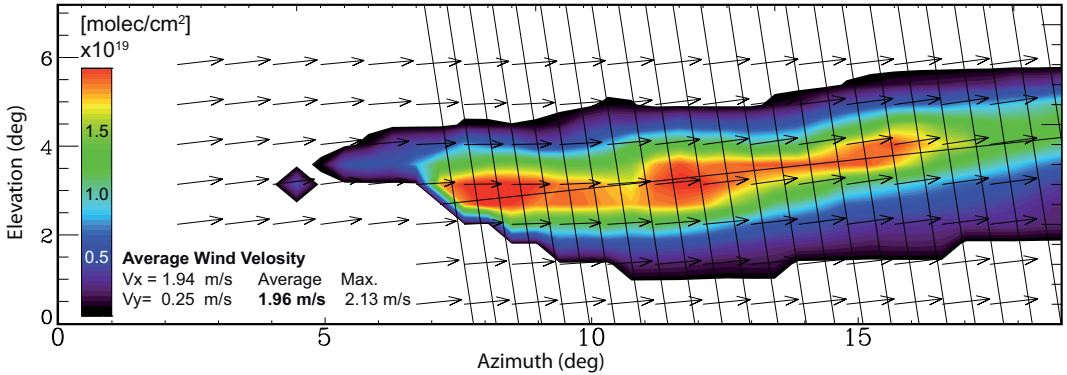

Fig. 3. Plume propagation vectors obtained from two sequential gas column images. SO_2 columns are retrieved from measured IR spectra asuming a temperature of 269 K at 5500 m a.s.l. obtained from a radiosonde at 06:00 a.m. The wind-field is retrieved from this and the following frame, solving the equation of continuity. The solid lines represent a linear aproximation for the trayectory and the cross-sections perpendicular to it. The corss-sections are separated by one minute intervals and the velocity of the propagating plume is projected to the drawn trajectory.

AMTD
5, 4599–4633, 2012

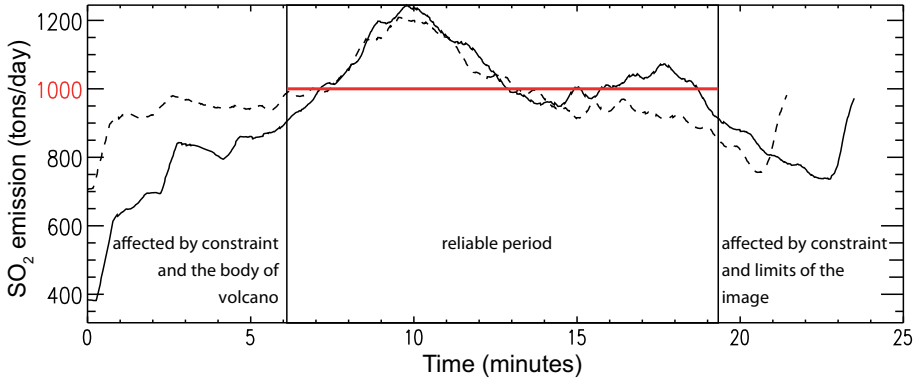

Fig. 4. Calculated SO_2 emission (tons day^{-1}) at different distances from the crater represented by the cross-sections drawn in Fig. 3 and using the reconstructed wind-field. The distance is shown as the time of its propagation after the starting point of the linear trajectory (Fig. 3). The solid trace shows the flux calulated using the first image of SO_2-columns and the dashed line is the flux at the same time, but based on the next SO_2-image. The reconstruction of the wind-field is done using a constraint which limits its spatial resolution. Especially near the crater, the dispersion of the SO_2 plume is not very well represented by the retrieved wind-field and the SO_2 emission/flux is underestimated (more or less below 6 min). A similar effect occurs at the other end of the image. In the center of the plume, where the linear trajectory is well represented, both SO_2-flux estimations are consistent and oscillate around 1000 tons day^{-1} in this case.

AMTD
5, 4599–4633, 2012

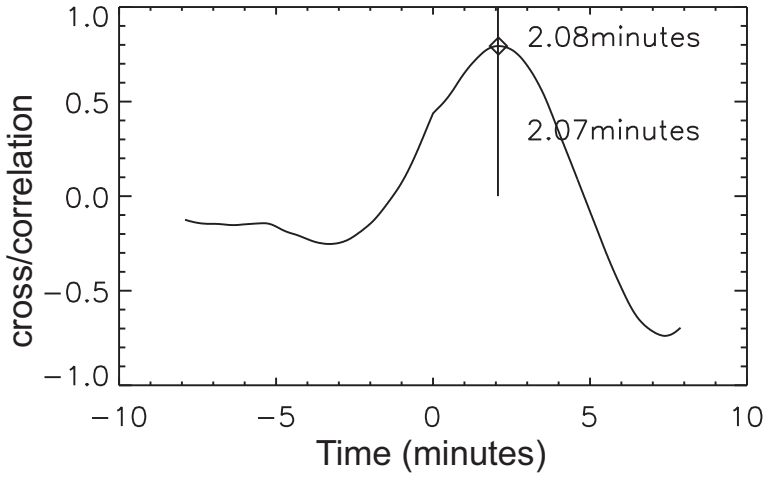

Fig. 5. The cross-correlation of the flux time-series in Fig. 4 shows a maximum corresponding to the delay between both frames. If the wind field is well retrieved, the delay obtained from this cross-correlation (diamond at the maximum after 2.08 min) should coincide with the known time delay between both measured frames (vertical line at 2.07 min). Normally, a small difference could always be expected since the wind-field result is smoothed and it is assumed that the plume does not change its direction of propagation, but larger discrepancies in the delays would mean that the wind-fields have not been properly retrieved.

AMTD
5, 4599–4633, 2012

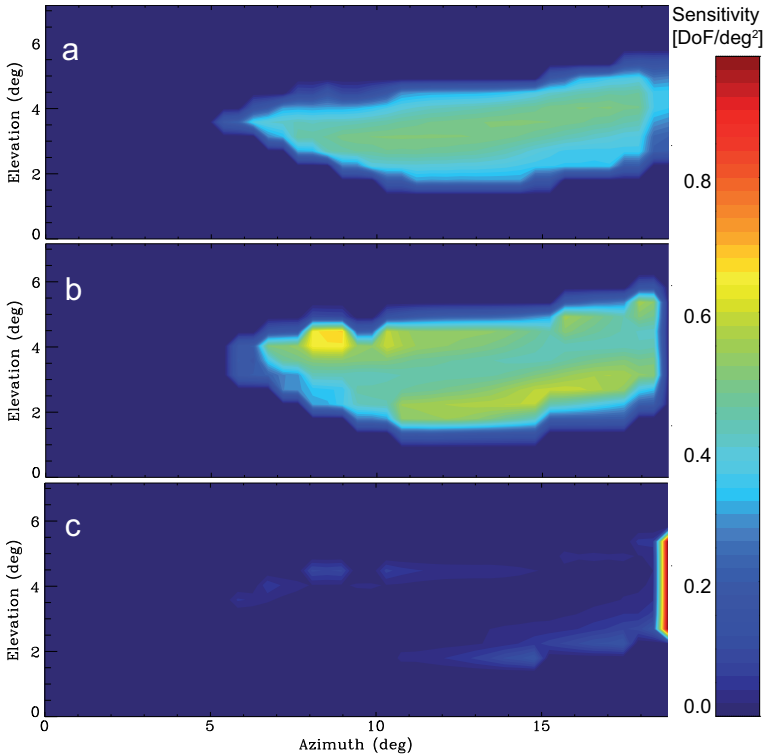

Fig. 6. Diagonal of the averaging kernel of the **(a)** x-($\mathbf{AK}_x$) and **(b)** y-wind velocity components ($\mathbf{AK}_y$), as well as of **(c)** the sources ($\mathbf{AK}_{\mathrm{src}}$). As the main wind direction is along the x-axis, $\mathbf{AK}_x$ represents the sensitivity to a deviation from the wind speed ($|v| - |\boldsymbol{v}_{\mathrm{a}}|$). This sensitivity regarding the wind-speed is also called $\mathbf{AK}_r$ in the text. As the main wind direction is along the x-axis, $\mathbf{AK}_y$ represents the sensitivity to a deviation from the wind direction ($\mathrm{d}\boldsymbol{v}_y = |\boldsymbol{v}_{\mathrm{a}}|\mathrm{d}\phi$). This sensitivity regarding the wind-direction is also called $\mathbf{AK}_\phi$ in the text. The sensitivity to sources depends on the constraint ($\mathbf{R}$) and the weighting of the measurements ($\mathbf{S}_{\mathrm{e}}^{-1}$).

AMTD
5, 4599–4633, 2012

Thermal emission spectroscopy of volcanic gases

A. Krueger et al.

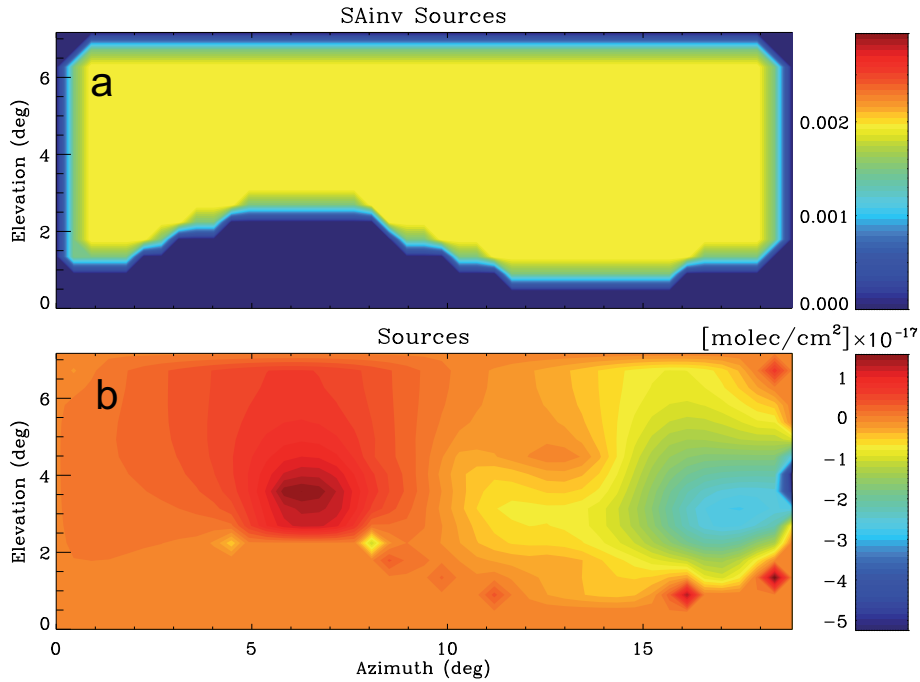

Fig. 7. (a) Diagonal of the regulation matrix concerning the strength of the sources. The units are arbitrary, they have to be compared with the constraint (**R**) concerning the wind components and with the weighting of the measurement ($\mathbf{S}_e^{-1}$) **(b)**. Retrieved sources are also part of the solution vector. As the wind-field is constrained, this additional fit-parameter improves the result significantly. The clean atmosphere is constrained with a smoothing constraint, while the pixels of the borders and the the volcanic body are constrained with an optimal-estimation-like regularization (**R**-matrix is diagonal). In this example, 11.7 independent pieces of information are included in the vector which has 714 elements to describe the sources. The retrieval finds the strongest sources above the crater.

AMTD
5, 4599–4633, 2012

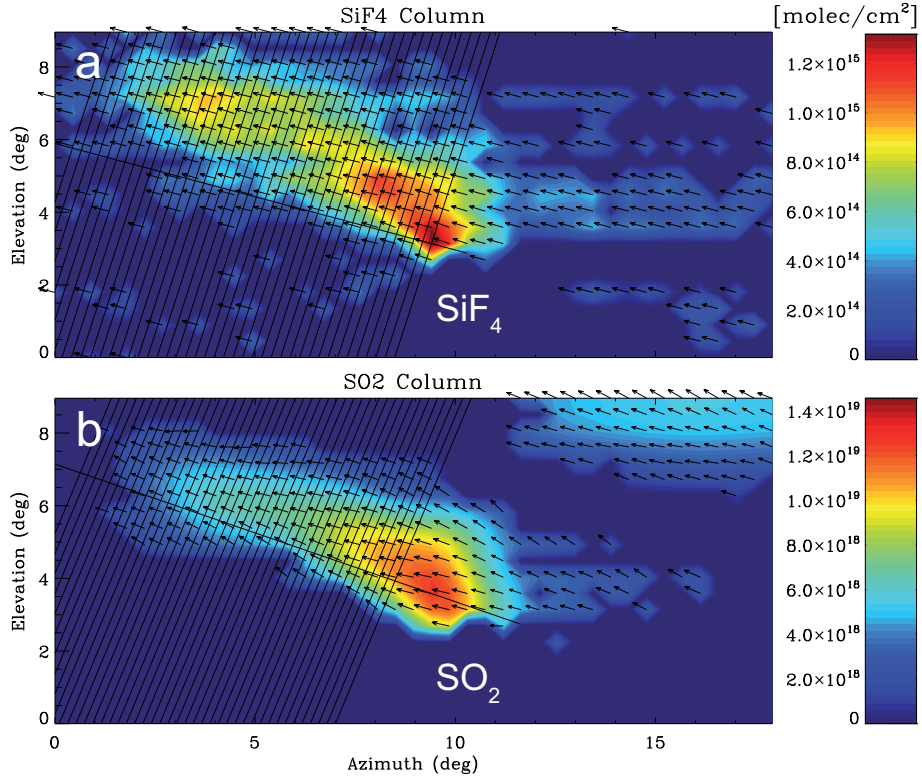

Fig. 8. Wind fields reconstructed from consecutive measurements of **(a)** SiF_4 and **(b)** SO_2. Even when the retrieved SiF_4 columns have rather large random errors and low precision, an average velocity can be obtained independently from the SO_2 plume retrieval. The retrieved wind speeds perpendicular to the line-of-sight from SiF_4 and SO_2 were found to be 0.8 $m\,s^{-1}$ and 0.7 $m\,s^{-1}$, respectively.

AMTD
5, 4599–4633, 2012